Supporting information

Converting Inorganic-Organic Hybrid Sulfides into Oxides: A General Strategy to Hierarchical-Porous-Structured Thermal-stable Metal Oxides with Improved Catalytic Performance

Yifu Yu, Shuangxia Hou, Ming Meng[*], Xutang Tao, Wenxian Liu, Youlei Lai, Bin Zhang[*]

Department of Chemistry, Tianjin Key Laboratory of Applied Catalysis Science & Engineering, School of Chemical Engineering & Technology and School of Science, Tianjin University, Tianjin 300072, P. R. China, and State Key Laboratory of Crystal Materials, Shandong University, Jinan 250100, P. R. China
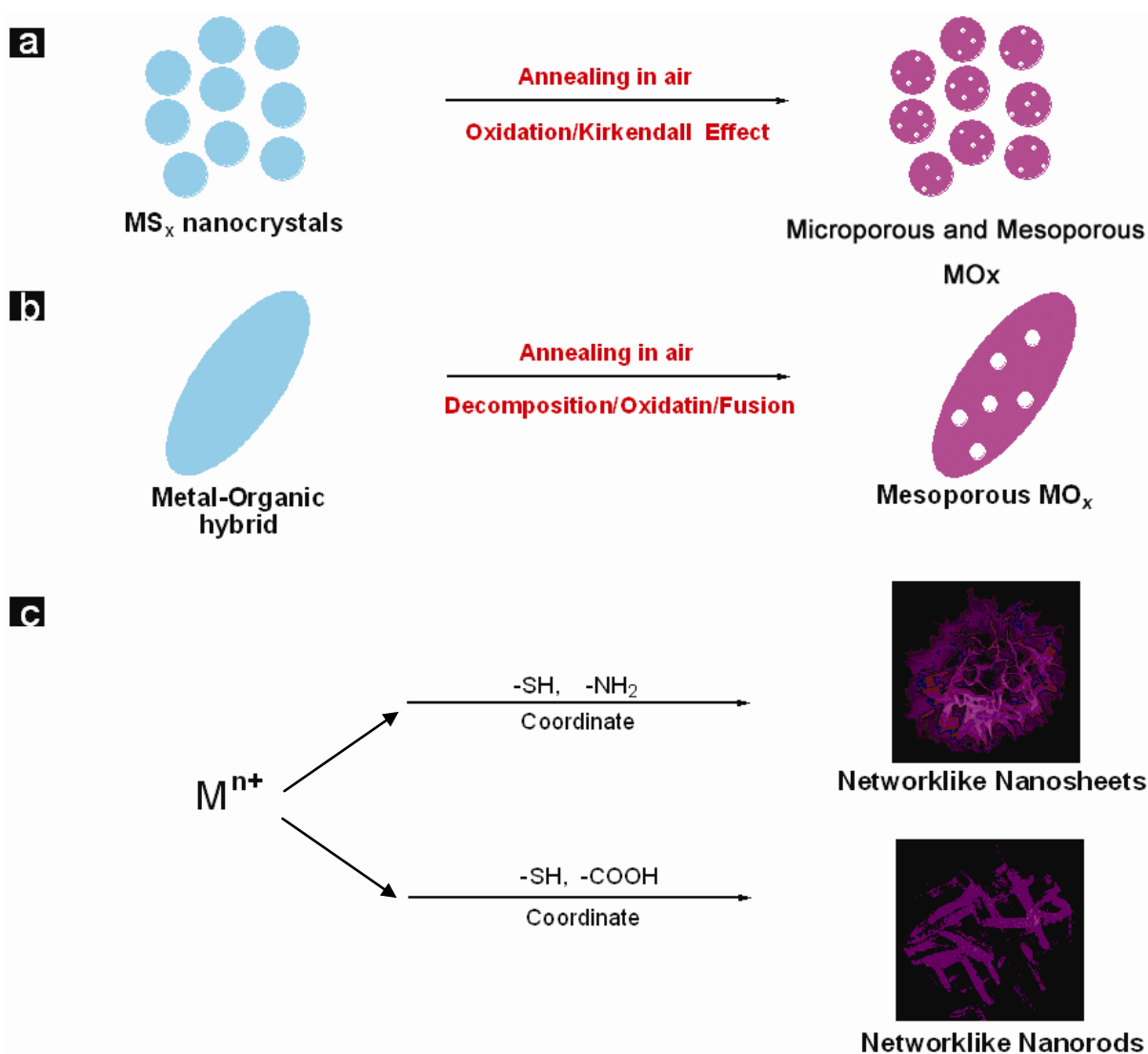E-mail: mengm@tju.edu.cn, bzhang@tju.edu.cn

Figure S1. a) Scheme illustrating the formation of micropores or hollow regions due to the Kirkendall effect when metal sulfides or metal were oxidized into oxides (*Science* 2004, **304**, 711-714; *Nature Materials* 2006, **5,** 627-631; *Angew. Chem. Int. Ed.* 2007, **46**, 4155-4162; *Chem. Mater.* 2009, **21**, 5237–5243; *J. Am. Chem. Soc.* 2008, **130**, 2736–2737; *Nano Lett.* 2010, **10,** 149–155.) b) Scheme showing the formation of mesopores when metal-organic hybrid nanostructures were thermally decomposed at high temperature (*Nano Res.* 2010, **3**, 81–91; *Adv. Funct. Mater.* 2007, **17**, 296–306; *Chem. Mater.* 2008, **20**, 4749–4755; *Adv. Funct. Mater.* 2008, **18**, 195–202; *J. Am. Chem. Soc.* 2009, **131**, 7486–7487). c) Scheme displaying the formation of flake-based structures with macropores or macroporous network-like sulfides prepared by the reaction of metal salts with molecules containing sulfhydryl, amido and carboxylic groups (*J. Phys. Chem. B* 2006, **110***, 8978–8985; *Adv. Funct. Mater.* 2008, **18**, 1194–1201). In this communication, we will combine the Kirkendall effect, the thermal decomposition and the controlled formation of macroporous sulfides into one designed strategy, and develop a general method to hierarchical-porous-structured oxides with micropores, mesopores and macropores by converting inorganic-organic hybrid sulfides into oxides.
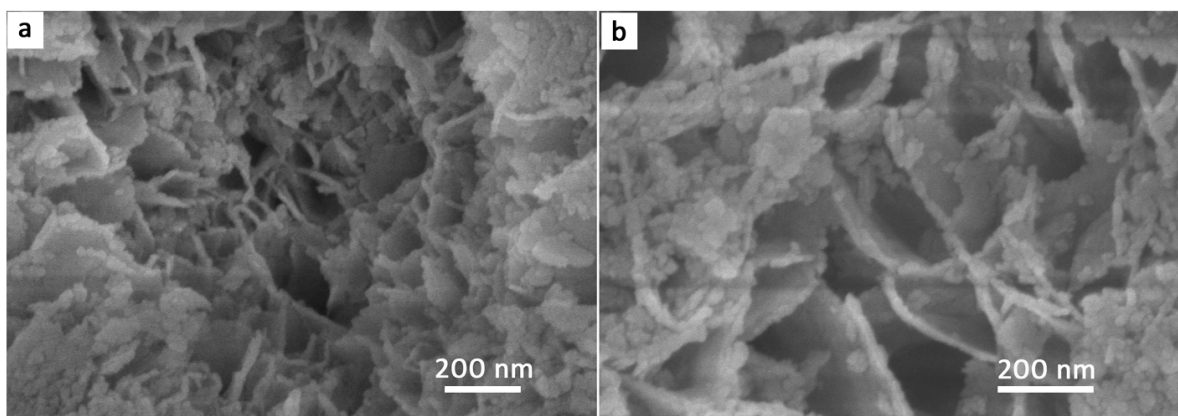
Figure S2. SEM images of the as-prepared hybrid precursors, suggesting that the inner parts are still composed of flakes rather than solid particles, and that macropores among flakes are still observed in the inner parts. This shows that the flake-based marcroporous configuration is filled in the whole sphere. This is important for the high surface area of CeO_2, and the high efficiency in utilizing the support for catalyst and the following catalytic reaction.
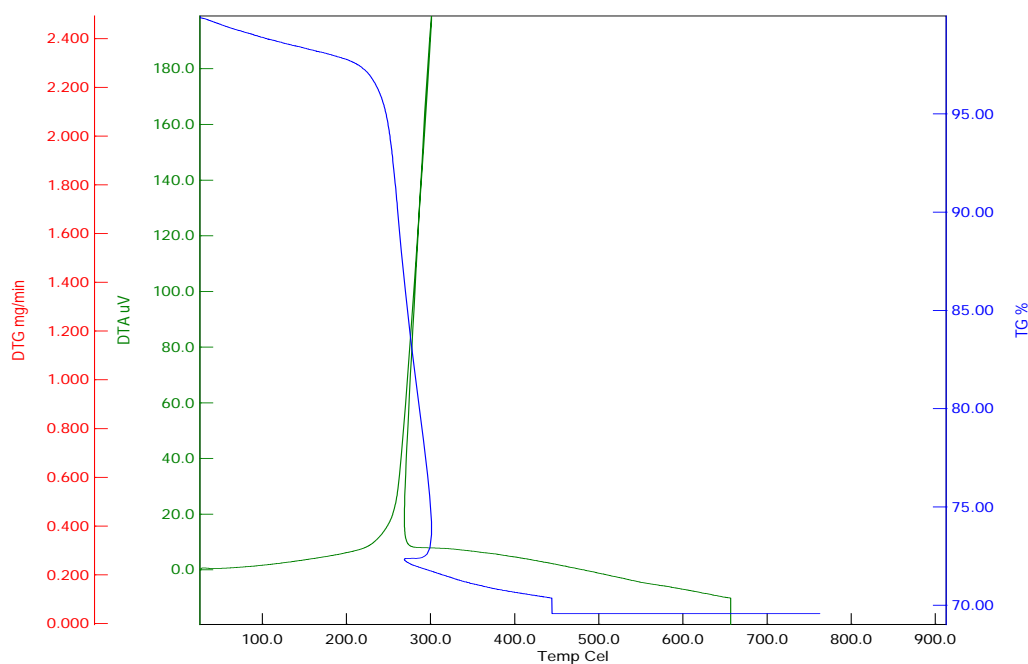
Figure S3. Thermogravimetric analysis (TGA) data of the hybrid precursors obtained in air. This shows that the oxidation and decomposition of the hybrid sulfide precursors in air started from 220 ºC, and almost finished at 300 ºC.
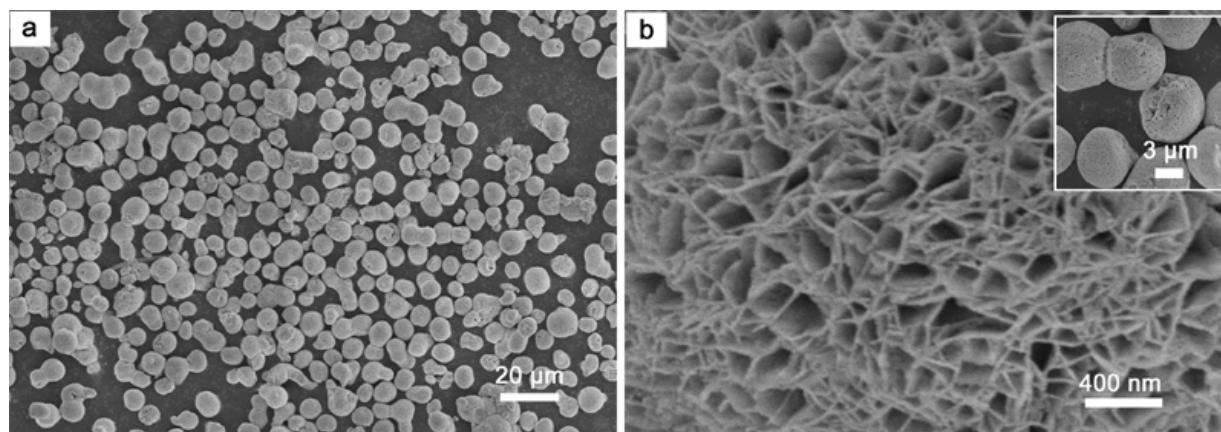

Figure S4. SEM images of the as-prepared HC3M obtained through the oxidation and thermal decomposition of the hybrid precursors at 500 ºC (HC3M-500). The size of macropores is obviously bigger that that of HC3M-300, suggesting that the temperature has exerted a noticeable influence on the pore size of HC3M.
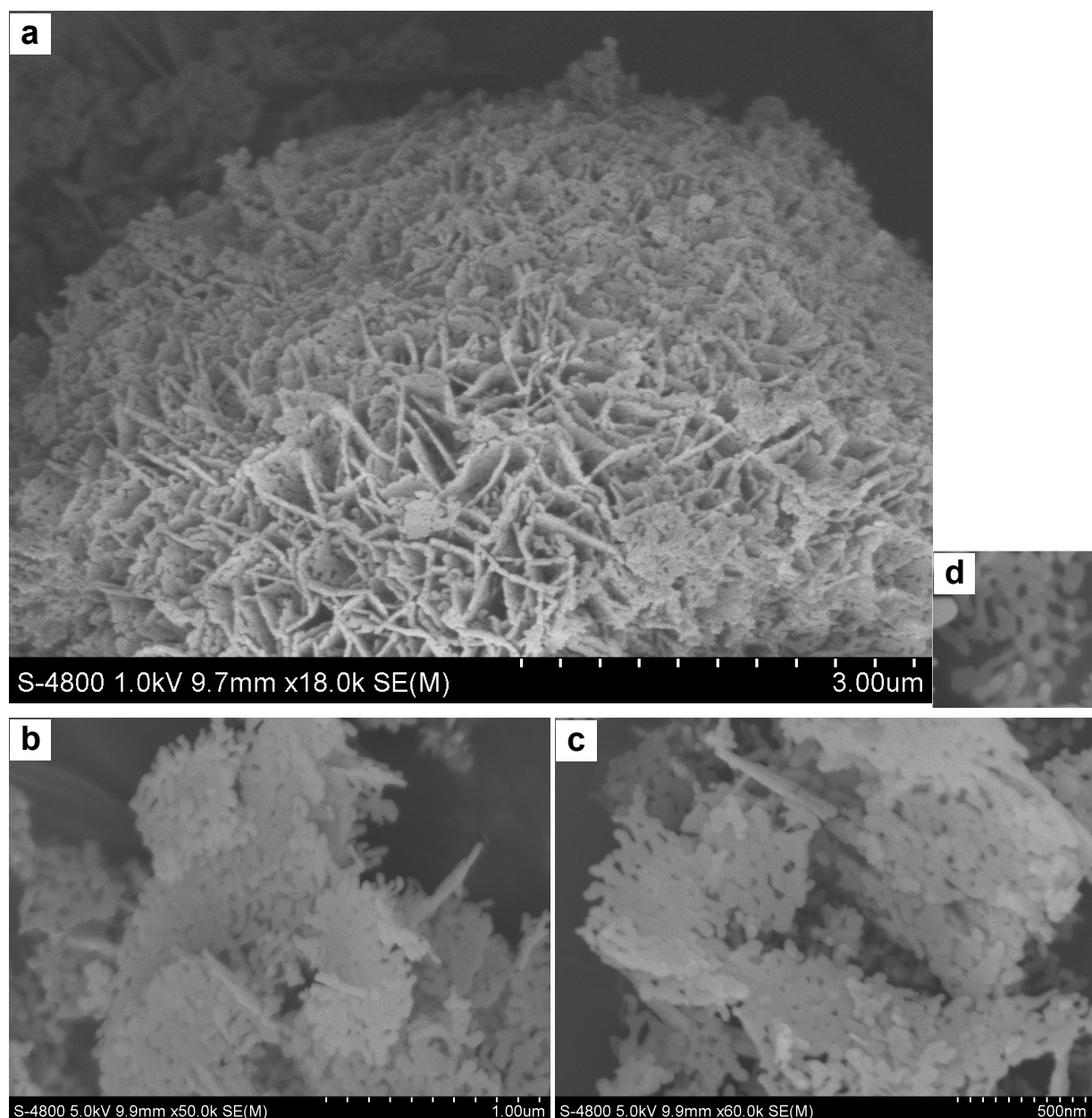
Figure S5. SEM images of the as-prepared HC3M obtained through the oxidation and thermal decomposition of the hybrid precursors at 800 ºC (HC3M-800), suggesting that the hierarchical-porous-structured CeO_2 microspheres are composed of particle-joined porous network-like flakes. Note that the as-prepared HC3M were sonicated for 30 min and then used for the SEM observations (Figure S5b,c,d).
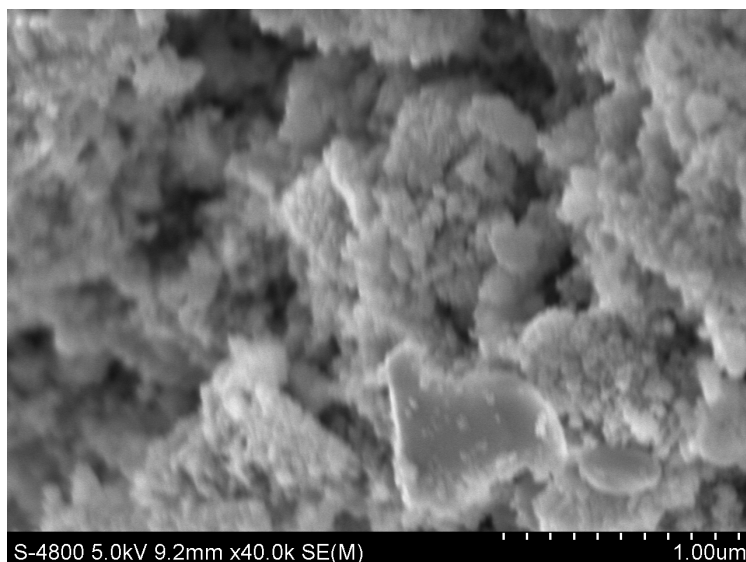
Figure S6. SEM image of CeO$_2$ nanoparticles prepared according to the reported sol-gel method (G. Qi, R. T. Yang, *J. Phys. Chem. B* 2004, **108**, 15738-15747).
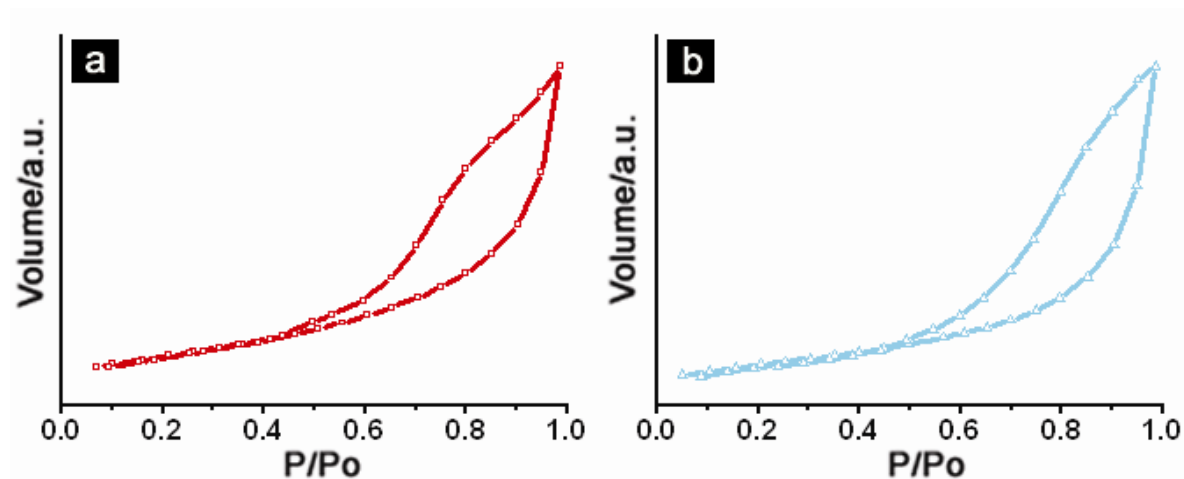

Figure S7. Nitrogen adsorption/desorption isotherms of mesopores of HC3M-500 (a) and HC3M-800 (b).

a

HC3M-300-Air
HC3M-300-Ar

dV/dD / cc^{-1}nm^{-1}g^{-1}

Pore Diameter / nm

b scale counts: 2087   Base(4)_pt10   Cursor: 0.000 keV
                                                                          0 Counts

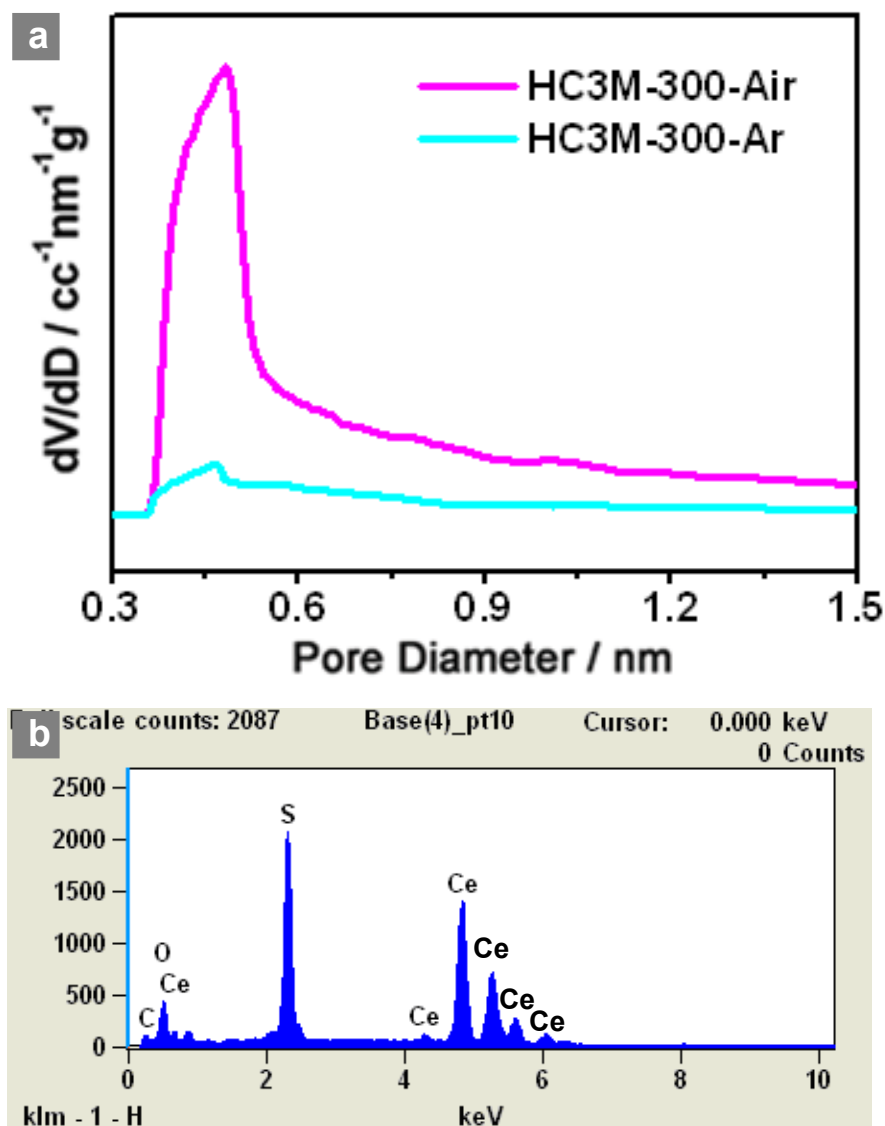klm - 1 - H   keV

Figure S8. Micropore diameter distributions (a) and EDX spectrum (b) of the as-prepared cerium sulfide obtained through the thermal decomposition of the hybrid precursors at 300 °C in Ar. No micropores were seen in the as-prepared cerium sulfide, obviously different from the microporous size distribution of HC3M-300. This reveals that the transformation of cerium sulfide into ceria in air or O_2 is important for the appearance of micropores in the final samples due to the Kirkendall effect. EDX spectrum indicates that the samples are composed of cerium and sulfur.

Table S1. BET surface area of mesopores of the porous CeO_2 obtained through the thermal decomposition of the hybrid precursor in Ar at 800 ºC and samples reported in references. The specific area of HC3M obtained at 800 ºC in air (Table 1) is obviously higher than that of porous CeO_2 through the annealing of the hybrid precursors in Ar. The improved surface area in air should be attributed to the formation of pores due to the Kirkendall effect during the transformation process of CeS_x into CeO_2.

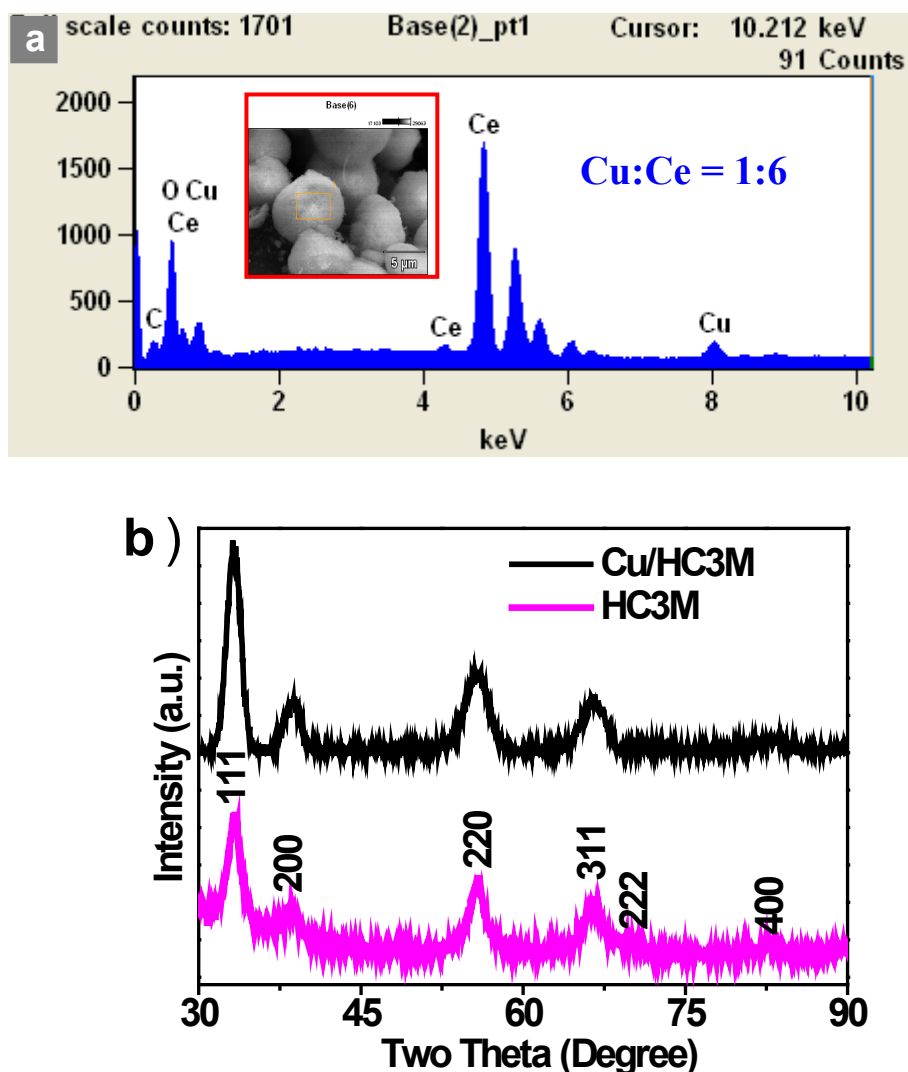| Samples	SEM images	A_{BET} (m^2/g)
Porous CeO_2 obtained through the thermal decomposition of the hybrid precursor in Ar at 800 ºC.	/	62
La-doped HC3M obtained at 300 ºC in air	Figure 4a	167
Porous CeO_2 microspheres	*J. Phys. Chem. B* 2006, **110**, 13445-13452	92.2
CeO_2 nanotubes synthesized using carbon nanotubes as the removable templates	*Micro. Meso. Mater.* 2009, **117**, 193–200	95.0

Figure S9. EDX spectrum (a) and the associated SEM image (the inset in Figure S9a), and XRD pattern of Cu/HC3M obtained through the impregnation of $Cu(NO_3)_2$ followed by being annealed at 300 °C for 4h. The EDX spectrum shows that the ratio of Cu to Ce is 1:6, which is in accordance with the molar ratio of $Cu(NO_3)_2$ to HC3M (1:5.7). This also suggests a final loading of 0.15 (Cu/Cu+Ce atom ratio) of Cu/HC3M. While in the XRD pattern of Cu/HC3M, any diffraction peaks from Cu, CuO and Cu_2O can not be detected, suggesting that Cu in HC3M is highly dispersed on CeO_2.
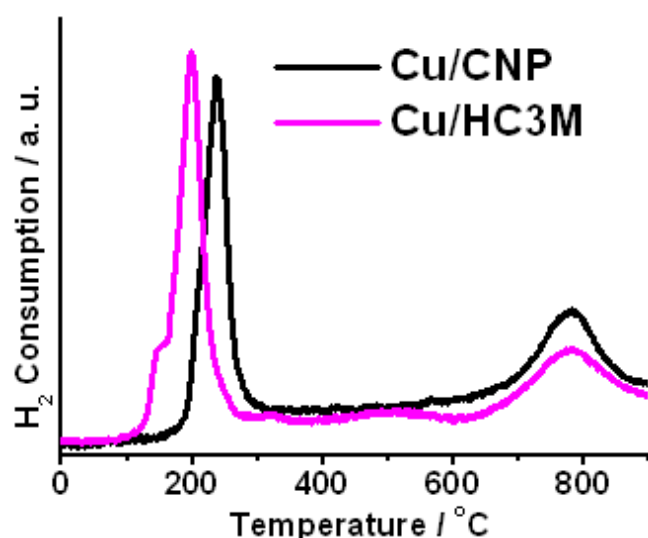
Figure S10. TPR curves of Cu/HC3M and Cu/CNP obtained under the same condition. The peaks at 800 °C can be attributed to the reduction of the bulk lattice oxygen of CeO_2, and the peaks between 150-400 °C can be attributed to the reduction of dispersed CuO supported on ceria. It is clearly found that the reduction peaks of CuO for Cu/HC3M and Cu/CNP are centered at 198 °C and 237 °C, respectively. This suggests that the size of the dispersed Cu on HC3M is much smaller as compared with that on Cu/CNP. In addition, a shoulder peak at 151 °C for Cu/HC3M (Figure S10) may originate from the strong interaction between Cu and CeO_2 (P. Larsson and A. Andersson, *Applied Catalysis B*, 2000, **24,** 175-192.). However, no shoulder peaks are observed in the TPR curve of Cu/CNP. Thus, the high catalytic activity of HC3M may be associated with the smaller copper species on HC3M and the stronger interaction between copper species and œria.
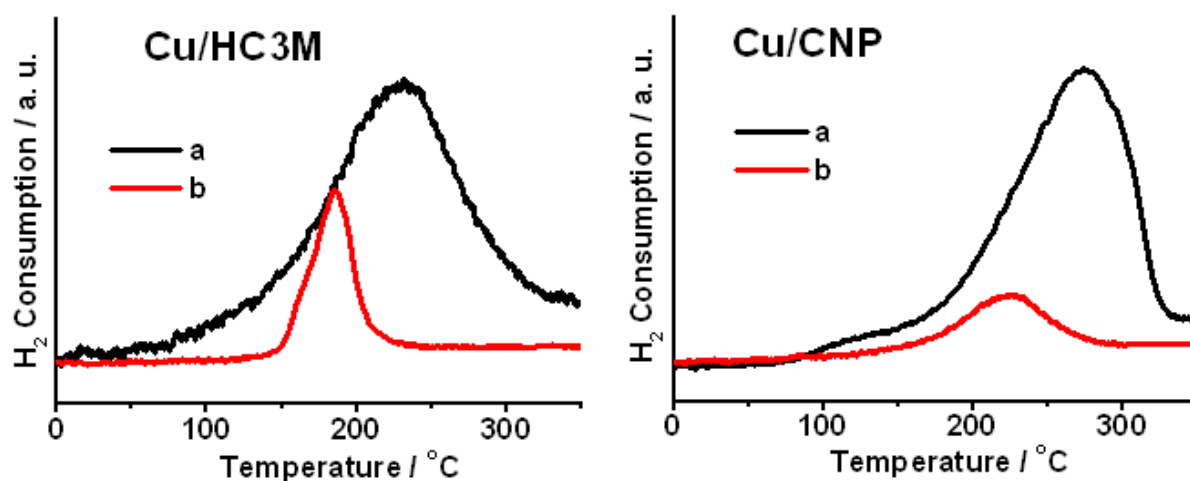

Figure S11. Reduction profiles of Cu/HC3M (left) and Cu/CNP (right). (a) TPR profile of the

different CeO_2 supported Cu catalysts and (b) profile of the second TPR of freshly oxidized Cu_2O phase after N_2O oxidation at 50 ^oC. According to the calculated hydrogen consumption in the TPR of the fresh ceria supported Cu catalysts (a) and in the second TPR of freshly oxidized surface Cu_2O phase after N_2O oxidation at low temperature (b), copper dispersion and exposed copper area can be calculated by equations adopted by van Der Grift and his coworkers (C. J. G. van Der Grift, A. F. H. Wielers, B. P. J. Jogh, J. van Beunum, M. M. Versluijs-Helder, J. W. Geus, *J. Catal.*, 1991, **131**, 178-189) and developed by Hou's group (Z. Yuan, L. Wang, J. Wang, S. Xia, P. Chen, Z. Hou, X. Zheng, *Appl. Catal. B: Environ.*, 2011, **101**, 431-430). The dispersion of copper in reduced Cu/HC3M and Cu/CNP is 45.5% and 31.0%, respectively.
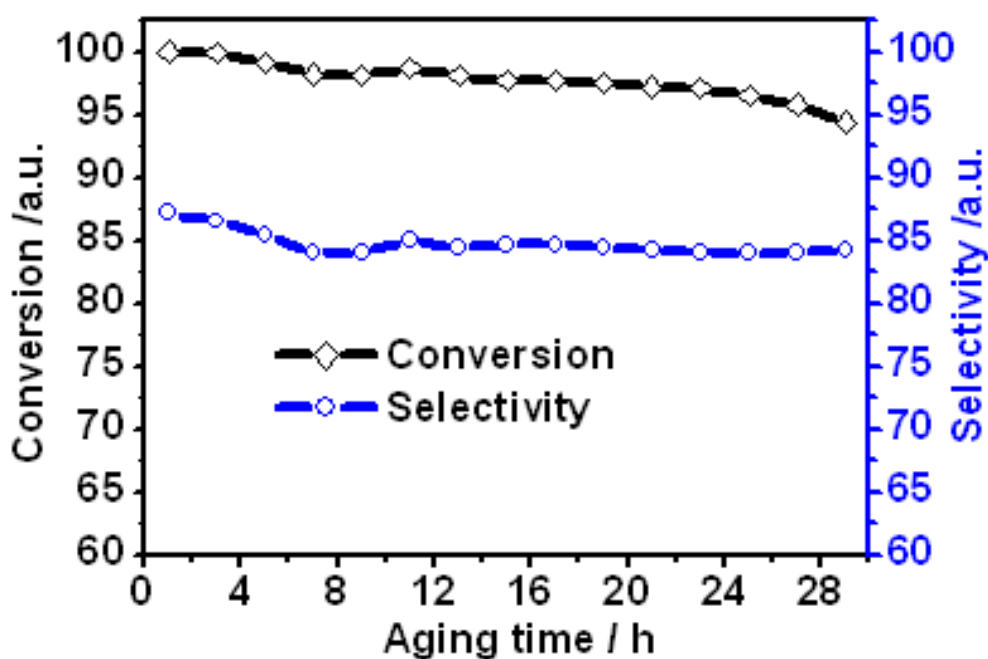

Figure S12. Aging curves of the catalytic activities of the CO conversion and selectivity to CO_2 selectivity of the as-prepared Cu/HC3M during CO PROX reaction which was carried out at 150 °C under the atmosphere of 1% CO, 1% O_2 and 50% H_2 (balanced by N_2) (200 mL min^{-1}). After continuous reaction for 29 h, the conversion is still more than 95%, and the selectivity is still higher than 80%, suggesting the high stability of the catalytic activity of the as-prepared Cu/HC3M.
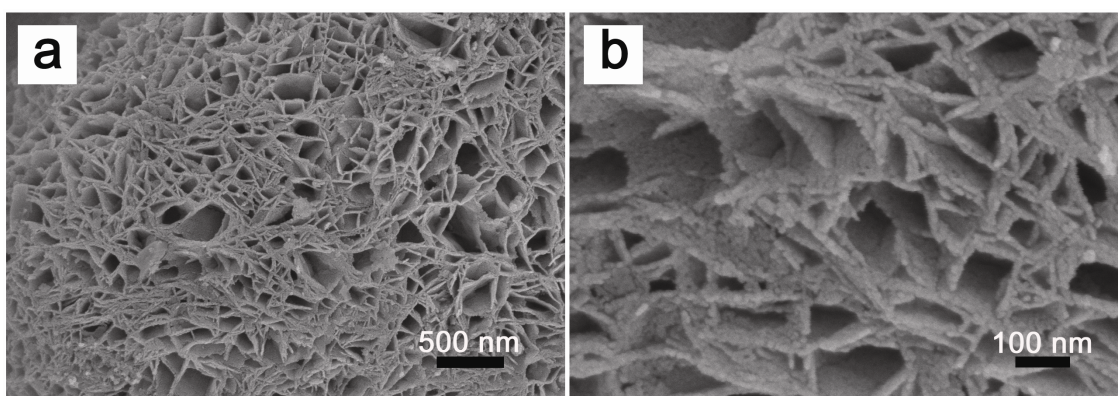
Figure S13. SEM images of the Cu/HC3M after experiencing a 29h-aging at 150 °C under the atmosphere of 1% CO, 1% O_2 and 50% H_2 (balanced by N_2) (200 mL min^{-1}). It is obvious that the macroporous and mesoporous structures of HC3M still exist, implying the high stability of the macropores and mesopores in Cu/HC3M.
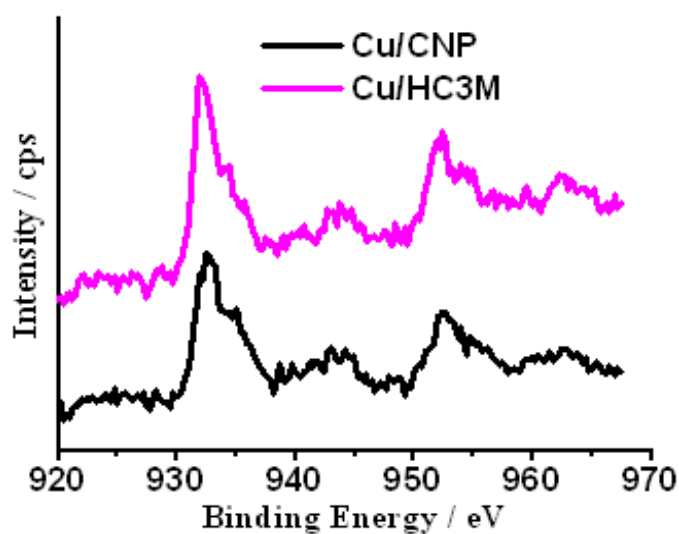

Figure S14. Cu2p XPS spectra of Cu/CNP and Cu/HC3M. No obvious differences are observed between the XPS spectra of Cu/HC3M and Cu/CNP.
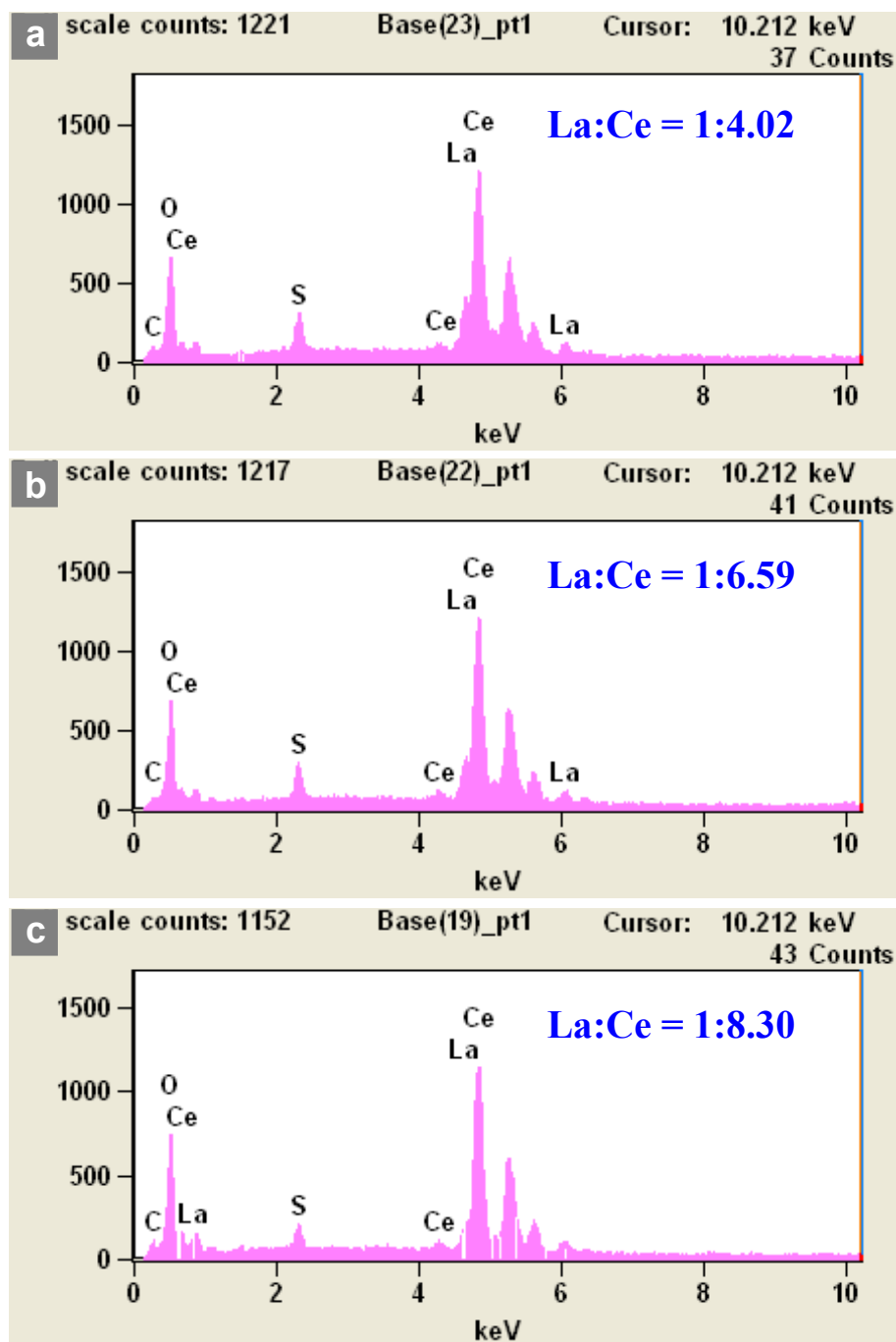
a scale counts: 1221   Base(23)_pt1   Cursor: 10.212 keV
                                                        37 Counts

La:Ce = 1:4.02

b scale counts: 1217   Base(22)_pt1   Cursor: 10.212 keV
                                                        41 Counts

La:Ce = 1:6.59

c scale counts: 1152   Base(19)_pt1   Cursor: 10.212 keV
                                                        43 Counts

La:Ce = 1:8.30

Figure S15. EDX spectra of La-doped Ce-based precursors obtained through the reaction between L-cysteine and the mixture of $Ce(OAc)_3$ and $La(NO_3)_3$ with different molar ratios at 200 °C for 19h. It is found that the amount of La in Ce-based precursors can be controlled by changing the relative ratio of $Ce(OAc)_3$ to $La(NO_3)_3$.

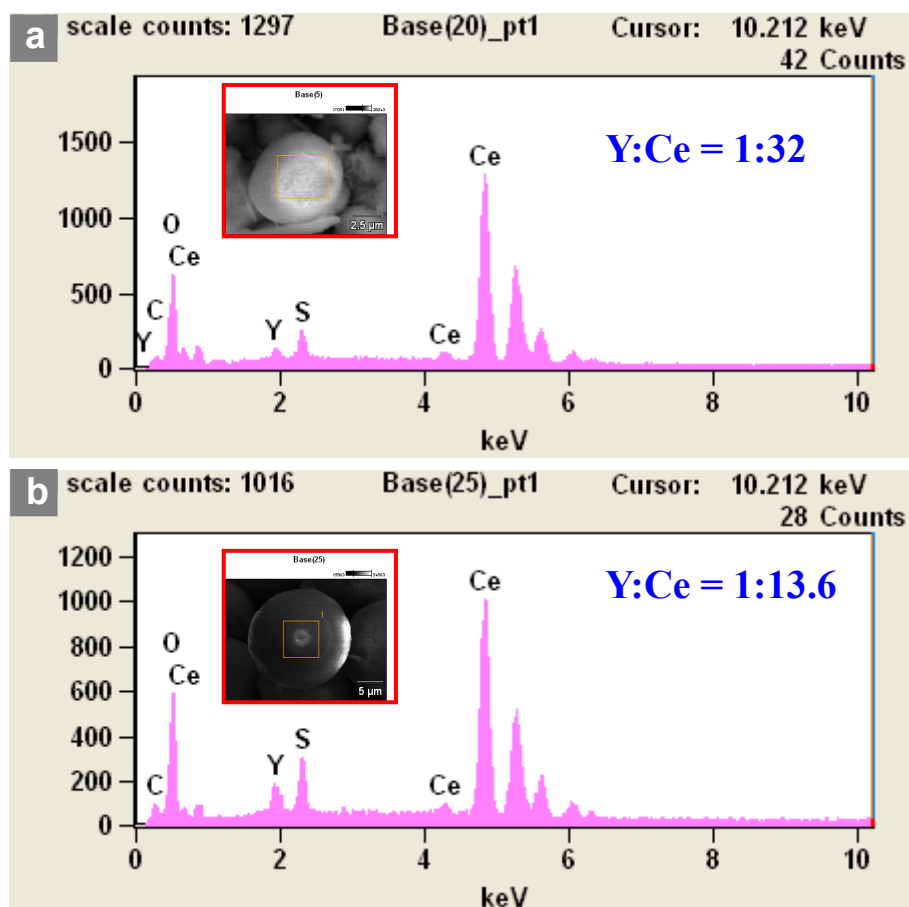**Figure S16.** EDX spectra of Y-doped Ce-based precursors obtained through the reaction between L-cysteine and the mixture of $Ce(OAc)_3$ and $Y(NO_3)_3$ with different molar ratios at 200ºC for 19h. It is found that the amount of Y in Ce-based precursors can be modulated by changing the relative ratio of $Ce(OAc)_3$ to $Y(NO_3)_3$.